



<b>Publication Year</b>	2024
<b>Acceptance in OA</b>	2025-02-10T11:17:23Z
<b>Title</b>	The MISTRAL Instrument and the Characterization of Its Detector Array
<b>Authors</b>	Paiella, A., Cacciotti, F., Isopi, G., Barbavara, E., Battistelli, E. S., de Bernardis, P., Capalbo, V., Carbone, A., CARRETTI, Ettore, Ciccalotti, E., Columbro, F., Coppolecchia, A., Cruciani, A., D'Alessandro, G., De Petris, M., GOVONI, Federica, Lamagna, L., Levati, E., MARONGIU, Pasqualino, MASCIA, Adina, Masi, S., MOLINARI, Emilio Carlo, MURGIA, MATTEO, NAVARRINI, Alessandro, Novelli, A., Occhiuzzi, A., ORLATI, ANDREA, Pappalardo, E., Pettinari, G., Piacentini, F., PISANU, Tonino, POPPI, Sergio, PORCEDDU, Ignazio Enrico Pietro, Ritacco, A., SCHIRRU, Maria Renata, VARGIU, GIAN PAOLO
<b>Publisher's version (DOI)</b>	10.1007/s10909-024-03210-1
<b>Handle</b>	<a href="http://hdl.handle.net/20.500.12386/35867">http://hdl.handle.net/20.500.12386/35867</a>
<b>Journal</b>	JOURNAL OF LOW TEMPERATURE PHYSICS
<b>Volume</b>	217



# The MISTRAL Instrument and the Characterization of Its Detector Array

A. Paiella<sup>1,2</sup> · F. Cacciotti<sup>1</sup> · G. Isopi<sup>1</sup> · E. Barbavara<sup>1</sup> · E. S. Battistelli<sup>1,2</sup> · P. de Bernardis<sup>1,2</sup> · V. Capalbo<sup>1</sup> · A. Carbone<sup>1</sup> · E. Carretti<sup>3</sup> · E. Ciccalotti<sup>1</sup> · F. Columbro<sup>1,2</sup> · A. Coppolecchia<sup>1,2</sup> · A. Cruciani<sup>2</sup> · G. D'Alessandro<sup>1,2</sup> · M. De Petris<sup>1,2</sup> · F. Govoni<sup>4</sup> · L. Lamagna<sup>1,2</sup> · E. Levati<sup>1</sup> · P. Marongiu<sup>4</sup> · A. Mascia<sup>4</sup> · S. Masi<sup>1,2</sup> · E. Molinari<sup>5</sup> · M. Murgia<sup>4</sup> · A. Navarrini<sup>4</sup> · A. Novelli<sup>1</sup> · A. Occhiuzzi<sup>1</sup> · A. Orlati<sup>3</sup> · E. Pappalardo<sup>1</sup> · G. Pettinari<sup>6</sup> · F. Piacentini<sup>1,2</sup> · T. Pisanu<sup>4</sup> · S. Poppi<sup>4</sup> · I. Porceddu<sup>4</sup> · A. Ritacco<sup>7</sup> · M. R. Schirru<sup>4</sup> · G. Vargiu<sup>4</sup>

Received: 2 November 2023 / Accepted: 26 August 2024 / Published online: 16 September 2024  
© The Author(s) 2024

## Abstract

The Millimeter Sardinia radio Telescope Receiver based on Array of Lumped elements KIDs, MISTRAL, is a cryogenic LEKID camera, operating in the W band (77–103 GHz) from the Gregorian focus of the 64-m aperture Sardinia Radio Telescope (SRT), in Italy. This instrument features a high angular resolution ( $\sim 12$  arcsec) and a wide instantaneous field of view ( $\sim 4$  arcmin), allowing continuum surveys of the mm-wave sky with many scientific targets, including observations of galaxy clusters via the Sunyaev–Zel’dovich effect. In May 2023, MISTRAL has been installed at SRT for the technical commissioning. In this contribution, we will describe the MISTRAL instrument focusing on the laboratory characterization of its focal plane: a  $\sim 400$ -pixel LEKID array. We will show the optical performance of the detectors highlighting the procedure for the identification of the pixels on the focal plane, the measurements of the optical responsivity and NEP, and the estimation of the optical efficiency.

---

✉ A. Paiella  
alessandro.paiella@roma1.infn.it

<sup>1</sup> Dipartimento di Fisica, Sapienza Università di Roma, Rome, Italy

<sup>2</sup> Istituto Nazionale di Fisica Nucleare, Sezione di Roma 1, Rome, Italy

<sup>3</sup> Istituto di Radioastronomia, Istituto Nazionale di Astrofisica, Bologna, Italy

<sup>4</sup> Osservatorio Astronomico di Cagliari, Istituto Nazionale di Astrofisica, Cagliari, Italy

<sup>5</sup> Osservatorio Astronomico di Brera & REM, Istituto Nazionale di Astrofisica, Merate, LC, Italy

<sup>6</sup> Istituto di Fotonica e Nanotecnologie, Consiglio Nazionale delle Ricerche, Roma, Italy

<sup>7</sup> Dipartimento di Fisica, Università di Roma Tor Vergata, Rome, Italy

**Keywords** MISTRAL · High angular resolution · LEKIDs · Optical performance

## 1 Science Case

High-angular-resolution observations in the microwave range offer a multitude of captivating astrophysical prospects. The detailed scrutiny of the Cosmic Microwave Background radiation empowers us to chart its anisotropies and examine galactic foregrounds at small angular scales. Furthermore, microwave observations, through the Sunyaev–Zel’dovich effect, afford a profound investigation of galaxy clusters, unveiling the intricacies of the intracluster medium and facilitating the exploration of shock and merger phenomena within these colossal celestial structures.

These high-angular-resolution observations also unlock a unique window to study large-scale structures: by dissecting the cosmic web, which encompasses filaments, voids, and the warm/hot intergalactic medium, we gain invaluable insights into the immense cosmic framework that molds our Universe.

Shifting our focus to galactic science, we gain the capacity to characterize regions of star formation, molecular clouds, and even the magnetic fields that permeate our Galaxy. We can also extend the analysis of the spectral energy distribution of extragalactic sources, encompassing active galactic nuclei, quasars, and radio galaxies, thereby enhancing our understanding of these cosmic entities.

Moreover, high-angular-resolution observations provide a promising avenue to confront a pressing challenge in contemporary astrophysics: the problem of the missing baryons [1].

## 2 The MISTRAL Instrument

The MISTRAL cryostat consists of a pulse tube cryocooler with helium lines about 100 m long [2], and a sub-kelvin Chase refrigerator<sup>1</sup> capable of cooling the focal plane below 250 mK for about 12 hours. The performance of the MISTRAL cryostat is described in [3].

The optical system, essential for relaying the Gregorian focus of the telescope to the detector array and selecting the W band, consists of a UHMW (ultra-high-molecular-weight polyethylene) window [4], a chain of quasi-optical filters<sup>2</sup> at different temperatures, a 4-K two-lens telecentric refractive system made in silicon with antireflection coating in Rogers 3003, and a 4-K cold stop aperture required to reduce the entrance pupil to a diameter of 60 m to avoid wavefront distortions induced by the shaped surfaces of the primary mirror of the telescope.

The detector technology chosen to populate the focal plane of MISTRAL is that of lumped element kinetic inductance detectors (LEKIDs) [5]. Kinetic inductance detectors (KIDs) [6] are pair-breaking detectors capable of detecting radiation with

<sup>1</sup> <https://www.chasecryogenics.com/products>.

<sup>2</sup> provided by QMC Instruments <https://www.chasecryogenics.com/products>.

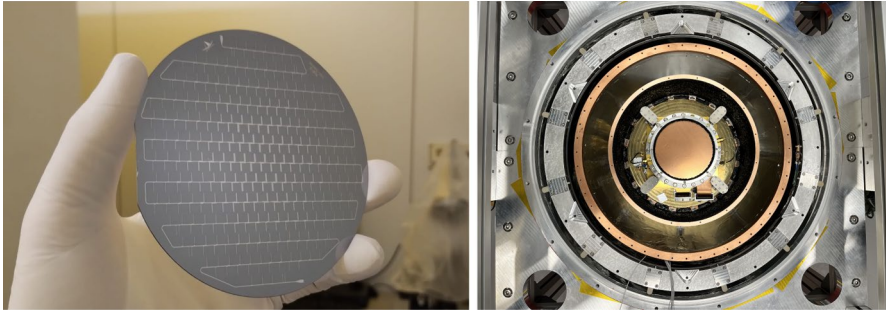


**Fig. 1** *Left panel:* picture of the 415-pixel LEKID array of MISTRAL. *Right panel:* picture of the detector holder closed by the 77–103 GHz band-pass filter mounted inside the MISTRAL cryostat

energy greater than the binding energy of Cooper pairs:  $2\Delta \approx 3.5k_B T_c$ , where  $T_c$  is the critical temperature of the superconducting film. The detector array consists of 415 LEKIDs, made of a titanium–aluminum bilayer [7–9], 10 + 30 nm thick, with a critical temperature of 945 mK [10]. The pixel absorbers are 3 mm × 3 mm in size, spaced by 4.2 mm which means an on-sky pixel separation of about 10.6 arcsec. They are directly coupled to the optical system. To prevent the feedline from altering its impedance due to incident radiation, it has been made of aluminum 21 nm thick, which features a critical temperature,  $T_c \approx 1.4$  K higher than that of the KIDs. Further details on the design and optimization of the MISTRAL detectors can be found in [10–12].

The detector array was fabricated at CNR-IFN, employing a lift-off lithographic procedure similar to that described in [13, 14]. The sample fabrication consisted of three subsequent lithographic steps: one for the realization of alignment markers (in Ti/Au) on the Si wafer, one for the realization of the KID array (in Ti/Al), and one for the realization of the feedline (in Al). Figure 1 shows a picture of the detector array, in the *left panel*, and a picture of the detector holder closed by the 77–103 GHz band-pass filter mounted inside the MISTRAL cryostat, in the *right panel*.

### 3 The Focal Plane Characterization

The electrical *dark* characterization of the MISTRAL array is extensively described in [12]. Here, we can find the measurements of the yield (85% at an operating temperature of 200 mK and 82% at an operating temperature of 245 mK), quality factors, electrical responsivity, and quasiparticle lifetime.

As for the optical characterization, we employed a calibrated W-band noise source connected to a horn with a 19-deg FWHM (full width at half maximum) beam, coupled to a NDF (neutral density filter) and a HDPE (high-density polyethylene) lens, resulting, at the focal plane surface, in an Airy disk with a diameter of approximately 10 mm. The NDF has been placed between the horn and the lens at a nonzero inclination angle to reduce standing waves, see the *right panel* of Fig. 2.

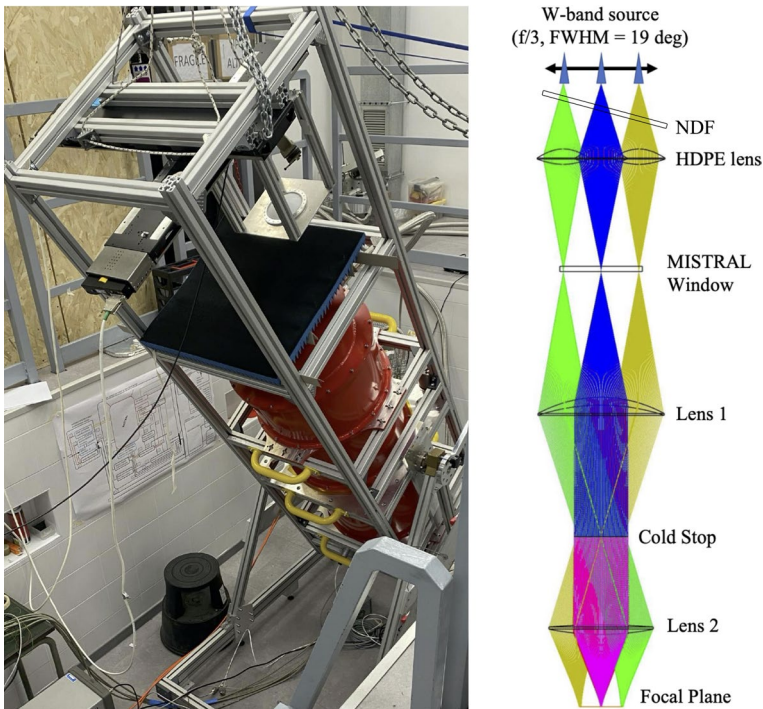


**Fig. 2** *Left panel:* picture of the calibration system composed of two linear stages, the W-band calibration source coupled to a horn (not visible in the picture), the NDF and the HDPE lens. *Right panel:* optical scheme of the calibration system

This configuration led to an over-illumination of the pixels, which, as said in sec. 2, are spaced 4.2 mm apart. By installing this entire setup on a two-linear-stage system to scan the entire focal plane, we proceeded with the pixel identification and optical responsivity measurements. A picture of this calibration system and the corresponding optical scheme are shown, respectively, in the *left* and *right* panel of Fig. 2.

### 3.1 Pixel Identification

In a densely packed KID array like that of MISTRAL, containing 415 resonators with a 500-MHz bandwidth, determining *a priori* which resonant frequency corresponds to a specific pixel is challenging. This is due to the fact that we do not achieve a 100% yield and because discrepancies always arise between the design and real-world implementation, including microfabrication issues, non-idealities, like parasitic inductance and capacitance, not accounted for in simulations, and so forth. Therefore, to ascertain the exact position of each pixel, identified by its resonant frequency, optical pixel identification becomes necessary. This procedure involves illuminating different regions of the focal plane while monitoring the response of all detectors, allowing us to create a mapping of the focal plane.

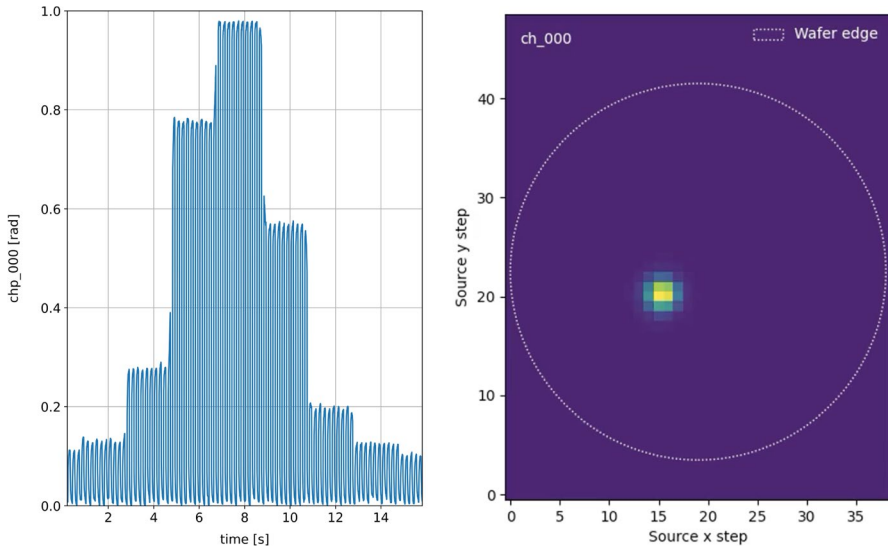


**Fig. 3** *Left panel:* time stream of the response of a representative detector (pixel 0) when illuminated by the modulated source emission scanning the focal plane. *Right panel:* map of the scanning source as observed by a representative detector (pixel 0)

Utilizing the system described earlier, we illuminated the entire focal plane by modulating the emission from the calibration source at a frequency of 10 Hz, and scanning with a spatial resolution of 2 mm, while employing a 2-s integration time per position.

The *left panel* of Fig. 3 shows a time stream for a representative detector recorded during a portion of the calibration source scan. We can observe the modulation of the signal emitted by the source, and the varying peak-to-peak amplitudes of the measured signal correspond to different source positions: each chunk of constant peak-to-peak amplitude lasts for 2 s, which is indeed the integration time selected for each source position. Moreover, each detector responds when illuminated by the source for multiple source positions because, as mentioned earlier, we over-illuminated the individual  $3\text{ mm} \times 3\text{ mm}$  wide pixels, which are spaced 4.2 mm apart, with a 10-mm-diameter beam.

Thus, by combining the time-streams with the source positions, it was possible to create maps depicting what each detector has observed, as illustrated for a representative pixel in the *right panel* of Fig. 3.

To determine the precise location of each pixel on the focal plane and estimate the corresponding signal, we fitted each pixel map with a two-dimensional Gaussian. The result for a representative pixel is shown in Fig. 4, where the *left panel* represents the measured map, the *central panel* is the Gaussian fit, and the *right panel* shows the residuals.

Having completed this process, we were able to proceed with the identification and mapping of the detectors on the focal plane. Figure 5 displays all the pixels found and identified at the two operating temperatures: 200 mK and 240 mK,

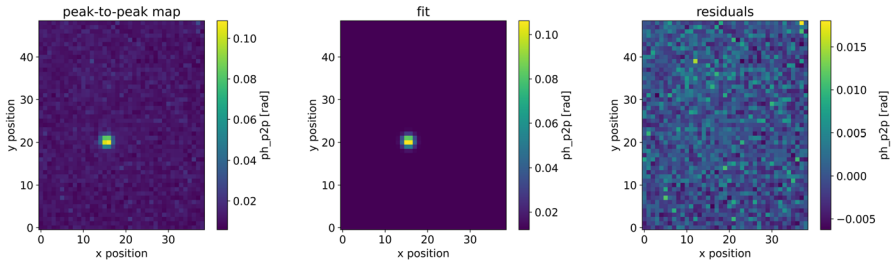


Fig. 4 Measured map (left panel), two-dimensional Gaussian fit (central panel), and residual map (right panel) for a representative detector (pixel 0)

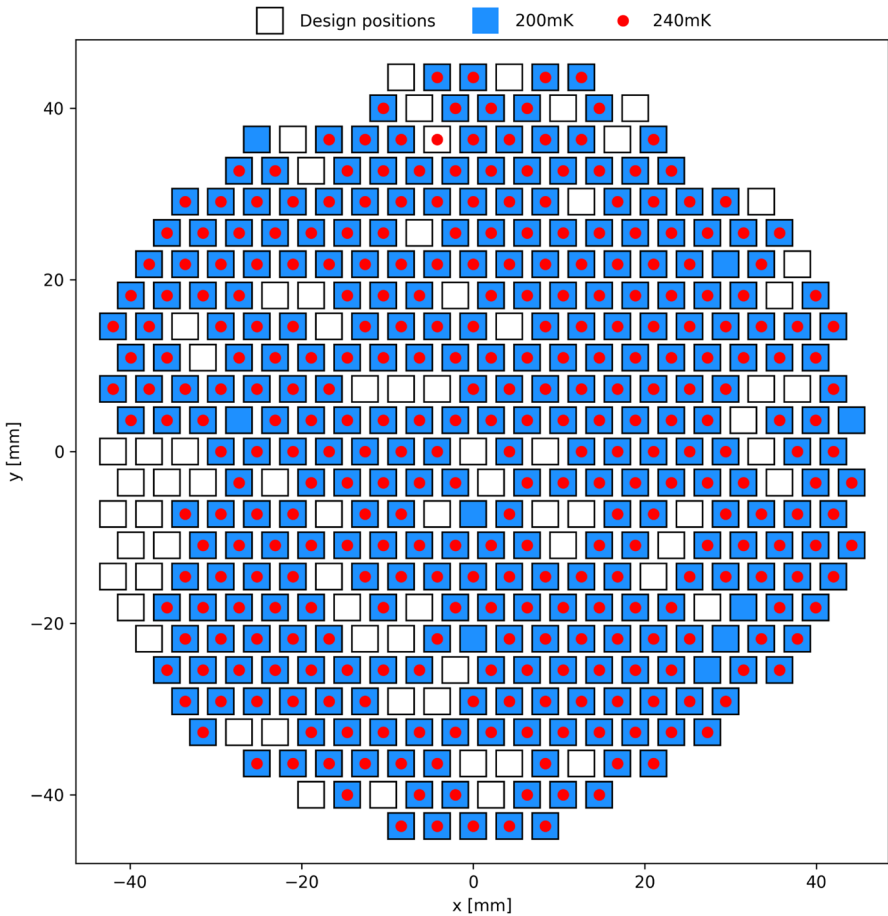
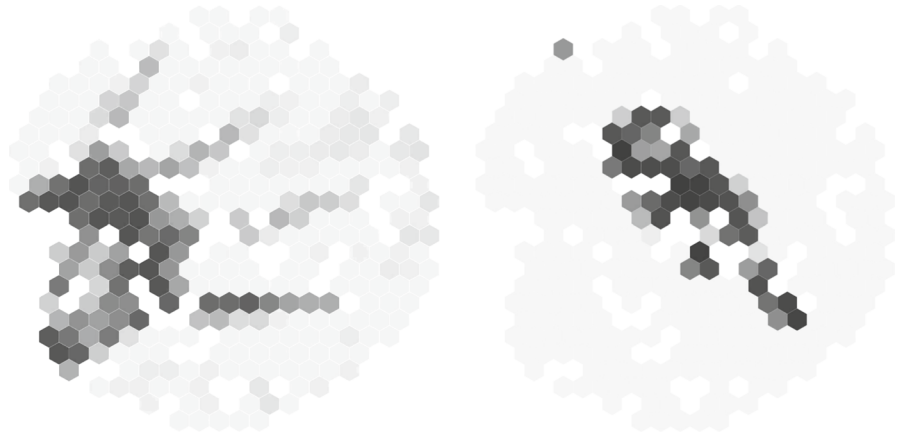


Fig. 5 Map of the operational pixels at 200 mK and 240 mK, compared to the design positions



**Fig. 6** Instantaneous images taken with the MISTRAL instrument: a hand in the *left panel*, and a bottle in the *right panel*

compared to the design positions. Compared to the yield measured under dark conditions, we identified 98% of the pixels at both temperatures, while in comparison with the design, we achieved an optical yield of 83% at 200 mK and 81% at 240 mK.

As an additional validation of the correct identification of the pixels on the focal plane, we recorded instantaneous images of a hand in the *left panel* of Fig. 6, and a bottle in the *right panel* of Fig. 6.

### 3.2 Responsivity, Noise Equivalent Power, and Optical Efficiency

The optical responsivity was estimated for each pixel by calculating the ratio between the peak of the two-dimensional Gaussian used to fit the signal, as described in the previous subsection, and the fraction of source power coupled to the corresponding pixel.

The noise equivalent power (NEP) was estimated for each pixel by calculating the ratio between the spectrum of the noise amplitude spectral density and the responsivity. The results for the NEP spectra of all the pixels are shown in the *left panel* of Fig. 7. Here, we highlighted three regions (centered at 2.5, 10, and 65 Hz), in *cyan*, where we evaluated the values of the NEP used for the histograms of the *right panel*.

In the NEP spectra, two lines at 1.8 and 3.6 Hz can be observed, originating from the pulse tube, likely due to suboptimal vibration damping system and resulting in an increase of the continuum spectrum of the NEP below 10 Hz. To confirm that both the two lines and the continuum below 10 Hz were indeed caused by the pulse tube, we turned off it and the results are presented in Fig. 8, where we observe the disappearance of the two lines and a reduction in the continuum compared to the case with the pulse tube on. That continuum part in the noise is caused by vibrations transmitted from the pulse tube to the laboratory MISTRAL structure. At SRT, MISTRAL will be anchored to a more massive structure, which will dampen the pulse tube vibrations, thereby reducing the noise [15].

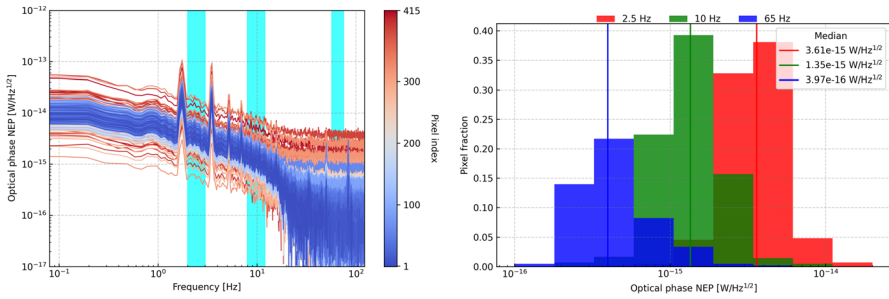


**Fig. 7** NEP in the case pulse tube on. *Left panel:* Spectra of the NEP for all the detectors. Different colors are for different pixels. The cyan regions indicate the values of the frequencies, centered at 2.5, 10, and 65 Hz, at which we assessed the NEP to construct the histograms. *Right panel:* histograms of the NEP evaluated in the three frequency regions

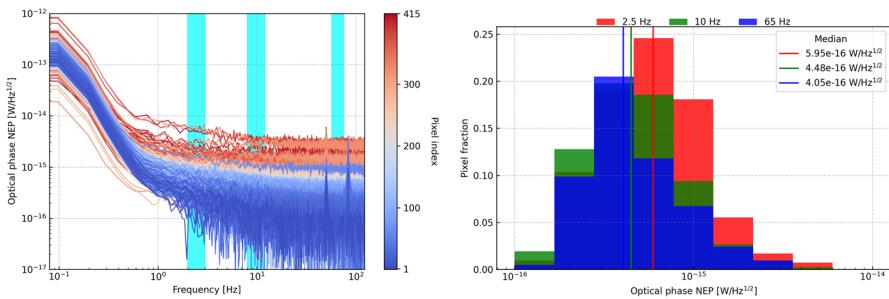


**Fig. 8** NEP in the case pulse tube off. *Left panel:* Spectra of the NEP for all the detectors. Different colors are for different pixels. The cyan regions indicate the values of the frequencies, centered at 2.5, 10, and 65 Hz, at which we assessed the NEP to construct the histograms. *Right panel:* histograms of the NEP evaluated in the three frequency regions

From the comparison between the cases with the pulse tube on and off, comparing the *right panels* of Figs. 7 and 8, we can observe that the NEP histograms evaluated around 65 Hz, which are away from the region affected by the pulse tube lines, are similar. Furthermore, in the case with the pulse tube off, the NEP histograms, evaluated in the three frequency regions, tend to overlap. In conclusion, we can infer that the NEP level of the detectors, unaffected by the pulse tube, is around  $5 \times 10^{-16} \text{W}/\sqrt{\text{Hz}}$ , below the expected photon noise level expected for MISTRAL at the Sardinia Radio Telescope of about  $1 \times 10^{-15} \text{W}/\sqrt{\text{Hz}}$ .

Lastly, by comparing the optical responsivity with the electrical responsivity measured in [12], we estimated a lower limit for the overall optical efficiency of the MISTRAL instrument around the 35%.

The on-sky sensitivity forecast, based on the laboratory measurements described here, and the map-making pipeline for the MISTRAL instrument coupled the Sardinia Radio Telescope are presented in [16], showing that MISTRAL can feature a noise equivalent flux density down to  $2.8 \text{mJy}/\sqrt{\text{Hz}}$

(assuming a telescope efficiency of 30%) and a mapping speed in the range  $170 - 1500 \text{ arcmin}^2/\text{mJy}^2/\text{h}$ , depending on the weather conditions.

## 4 Conclusion

In this paper, we described the laboratory characterization of the MISTRAL focal plane, discussing the procedure for the pixel identification, the estimation of the optical responsivity and NEP, and the evaluation of the overall optical efficiency. The optimal performance of the detectors, together with the proper functioning of the MISTRAL cryogenic and optical systems, has led to the green light for the installation of MISTRAL at the telescope.

In May 2023, the MISTRAL instrument was successfully installed at the Sardinia Radio Telescope: the MISTRAL cryostat, the detector readout electronics and all the housekeeping equipment at the Gregorian focus, the compressor of the pulse tube in the compressor room, about 100 m far from the cryostat, and the housekeeping and readout PCs in the control room.

MISTRAL is expected to see its first light soon, and from there, the scientific commissioning phase will begin. At the conclusion of the commissioning phase, MISTRAL will be available for observation proposals as a facility instrument of SRT. The remarkable capabilities of high-angular-resolution observations of the microwave sky with a wide instantaneous field of view, offer an unprecedented opportunity to unravel the mysteries of the Cosmos. Through the exploration of the CMB, galaxy clusters, large-scale structures, galactic phenomena, and extragalactic sources, we take steps toward a more profound understanding of the Universe and tackle open questions in astrophysics including the quest for missing baryons.

**Funding** Open access funding provided by Università degli Studi di Roma La Sapienza within the CRUI-CARE Agreement.

**Open Access** This article is licensed under a Creative Commons Attribution 4.0 International License, which permits use, sharing, adaptation, distribution and reproduction in any medium or format, as long as you give appropriate credit to the original author(s) and the source, provide a link to the Creative Commons licence, and indicate if changes were made. The images or other third party material in this article are included in the article's Creative Commons licence, unless indicated otherwise in a credit line to the material. If material is not included in the article's Creative Commons licence and your intended use is not permitted by statutory regulation or exceeds the permitted use, you will need to obtain permission directly from the copyright holder. To view a copy of this licence, visit <http://creativecommons.org/licenses/by/4.0/>.

## References

1. A.D. Hincks et al., A high-resolution view of the filament of gas between Abell 399 and Abell 401 from the Atacama Cosmology Telescope and MUSTANG-2. *Mon. Not. Roy. Astron. Soc.* **510**(3), 3335–3355 (2021). <https://doi.org/10.1093/mnras/stab3391>
2. A. Coppolecchia et al., Pulse tube cooler with > 100 m flexible lines for operation of cryogenic detector arrays at large radiotelescopes. *J. Low Temp. Phys.* **211**, 415–425 (2023). <https://doi.org/10.1007/s10909-022-02934-2>

3. A. Coppolecchia, et al., Cryogenic performance of the MISTRAL instrument. *J. Low Temp. Phys.* (This Special Issue) (2024)
4. G. D'Alessandro et al., Ultra high molecular weight polyethylene: optical features at millimeter wavelengths. *Infrared Phys. Technol.* **90**, 59–65 (2018). <https://doi.org/10.1016/j.infrared.2018.02.008>
5. S. Doyle et al., Lumped element kinetic inductance detectors. *J. Low Temp. Phys.* **151**, 530–536 (2008). <https://doi.org/10.1007/s10909-007-9685-2>
6. P. Day et al., A broadband superconducting detector suitable for use in large arrays. *Nature* **425**, 817–821 (2003). <https://doi.org/10.1038/nature02037>
7. A. Catalano et al., Bi-layer kinetic inductance detectors for space observations between 80–120 GHz. *Astron. Astrophys.* **580**, 15 (2015). <https://doi.org/10.1051/0004-6361/201526206>
8. A. Paiella et al., Development of lumped element kinetic inductance detectors for the W-band. *J. Low Temp. Phys.* **211**, 415–425 (2016). <https://doi.org/10.1007/s10909-015-1470-z>
9. B. Aja et al., Bi-layer kinetic inductance detectors for W-band. *IEEE/MTT-S Int. Microw. Sympos. (IMS)* **2020**, 932–935 (2020). <https://doi.org/10.1109/IMS30576.2020.9223828>
10. A. Paiella et al., MISTRAL and its KIDs. *J. Low Temp. Phys.* **209**, 889–898 (2022). <https://doi.org/10.1007/s10909-022-02848-z>
11. A. Coppolecchia et al., W-band lumped element kinetic inductance detector array for large ground-based telescopes. *J. Low Temp. Phys.* **199**, 130–137 (2020). <https://doi.org/10.1007/s10909-019-02275-7>
12. F. Cacciotti, et al., Dark performance of the MISTRAL LEKIDs. *J. Low Temp. Phys.* (This Special Issue) (2024)
13. A. Paiella et al., Kinetic inductance detectors for the OLIMPO experiment: design and pre-flight characterization. *J. Cosmol. Astropart. Phys.* **2019**(01), 039 (2019). <https://doi.org/10.1088/1475-7516/2019/01/039>
14. A. Paiella et al., Total power horn-coupled 150 GHz LEKID array for space applications. *J. Cosmol. Astropart. Phys.* **2022**(06), 009 (2022). <https://doi.org/10.1088/1475-7516/2022/06/009>
15. A. Paiella, et al., The W-band LEKID array of the MISTRAL instrument. *Proc. SPIE 13102, Millimeter, Submillimeter, and Far-Infrared Detectors and Instrumentation for Astronomy XII, 131020C* (16 August 2024). <https://doi.org/10.1117/12.3018301>
16. G. Isopi, et al., MISTRAL: science perspectives and performance forecasts. *J. Low Temp. Phys.* (This Special Issue) (2024)

**Publisher's Note** Springer Nature remains neutral with regard to jurisdictional claims in published maps and institutional affiliations.